

Electronic Supporting Information

Making Prussian blue analogues nanoparticles luminescent: effect of the luminophore confinement over the properties.

Ekaterina Mamontova,^a Jérôme Long*,^a Rute A. S. Ferreira,^b Alexandre M. P. Botas,^b Fabrice Salles,^c Yannick Guari,^a Luis D. Carlos^b and Joulia Larionova^a

a. Institut Charles Gerhardt, Equipe Ingénierie Moléculaire et Nano-Objets, Université de Montpellier, ENSCM, CNRS. Place Eugène Bataillon, 34095 Montpellier Cedex 5, France, E-mail : jerome.long@umontpellier.fr

b. Department of Physics and CICECO - Aveiro Institute of Materials, University of Aveiro, 3810-193, Aveiro, Portugal.

c. Institut Charles Gerhardt, Equipe Agrégats, Interfaces et Matériaux pour l'Energie, ENSCM, CNRS, Université de Montpellier. Place Eugène Bataillon, 34095 Montpellier Cedex 5, France.

Table of Contents

Synthetic procedures.....	4
Characterisation methods.....	4
Computational section	6
Fig. S1. IR spectra of 1 (left) and comparison between IR spectra of AA, 1 and 1@AA (right).	7
Fig. S2. PXRD patterns of 1 (black) and 1@AA (red).	7
Fig. S3. TEM image (left) and size distribution (right) for 1.	7
Fig. S4. Left: TGA analysis obtained with a 5°C.min ⁻¹ heating rate for 1, AA and 1@AA. Right: TGA curve obtained with a 5°C.min ⁻¹ heating rate demonstrating the decomposition of 1@AA.....	8
Fig. S5. SEM image for 1 (left) and 1@AA (right).	8
Fig. S6. Pore size distribution of 1 obtained from Monte Carlo simulations illustrating the presence of two types of pores corresponding to the channels and the larger pores formed by the vacancies.	8
Fig. S7. Top: Snapshot illustrating the density of presence of the AA molecules in the empty PBA structure 1 from Monte Carlo simulations. Bottom: Plausible Configuration of the AA molecule in PBA structure 1 from Monte Carlo simulations at low coverage.	9
Fig. S8. ZFC/FC curves performed for 1 with an applied magnetic field of 100 Oe (left); ZFC curves performed with an applied magnetic field of 100 Oe for 1 and 1@AA (right). ..	10
Fig. S9. Field dependence of the magnetization performed at 2.5K for 1 and 1@AA.	10
Fig. S10. Room temperature absorption spectra for AA and 1@AA in ethanol (1 mg/mL).	10
Fig. S11. Photographs of 1 (left) and 1@AA (right) re-dispersed in ethanol and excited under a UV lamp, wavelength 365 nm.	11
Fig. S12. Left: Room temperature normalized emission spectra for 1@AA re-dispersed in ethanol or water (1 mg/mL) and excited at 370 nm. Right: Room temperature normalized excitation spectra for AA and 1@AA re-dispersed at various concentrations in ethanol. ...	11
Fig. S13. Excitation and emission spectra monitored around 500 nm and excited at 365 nm, respectively, acquired at (left) 300 K and (right) 16 K for powdered AA and 1@AA; ΔE indicates the energy difference between the high-wavelength component in the excitation spectra and the singlet emitting state.	12
Fig. S14. Room temperature emission (left) and excitation (right) spectra for powdered 1@AA.	12
Fig. S15. Room temperature emission (left) and excitation (right) spectra for powdered AA.	13
Fig. S16. Emission spectra excited at 274 nm and excited at 365 nm of powdered AA as function of temperature.	13
Fig. S17. Excitation spectra monitored at 500 nm of powdered AA as function of temperature	14
Fig. S18. Emission spectra excited at 290, 360 and 432 nm for powdered 1@AA as function of temperature	15

Fig. S19. Excitation spectra monitored at 485 and 505 nm of powdered 1@AA as function of temperature.	16
Fig. S20. Integrated intensity of the emission (left) and excitation spectra (right) excited at 360-365 nm and monitored at 485-500 nm, respectively for powdered AA and 1@AA. The solid lines are guide to the eyes.	17
Fig. S21. Emission decay curves of powdered AA monitored at 500 nm as function of temperature. The solid lines represent the data best ($r>0.9$) fit using a single exponential function. The insets show the fit residual plots.....	18
Fig. S22. Emission decay curve of powdered 1@AA monitored at 500 nm as function of temperature. The solid lines represent the data best ($r>0.9$) fit using a single exponential function. The insets show the fit residual plots.....	19
Fig. S23. a) Thermal dependence of the fluorescence lifetime values for powdered AA (black) and 1@AA (red) monitored at 500 nm. The solid lines correspond to the data best fit using the Mott-Seitz model (Equation (1)); b) Fit regular residual plot.	20
Table S1. Values of the zeta potential for 1 and 1@AA.....	20

Experimental section

Synthetic procedures

Materials. All chemical reagents were purchased and used without further purification: Nickel(II) chloride hexahydrate (Alfa Aesar, 98%), Potassium hexacyanochromate (III) (Aldrich, 99.99%), 2-aminoanthracene (Alfa Aesar, 94%), ultra-pure water, ethanol 96% vol (TechniSolv), SnakeSkin Dialysis Tubing (3,5000 MWCO, 22 mm × 35 feet dry diameter, 34 mm dry flat width, ThermoScientific).

Synthesis of $K^+/Ni^{2+}/[Cr^{III}(CN)_6]^{3-}$ PBA nanoparticles (1). At 25 °C, aqueous solutions of $NiCl_2 \cdot 6H_2O$ (8 mM, 50 mL) and $K_3[Cr(CN)_6]$ (9 mM, 50 mL) were added simultaneously to 100 mL of pure water at 1.5 mL.min⁻¹ rate, using a syringe pump. After addition, the mixture was stirred one hour before being centrifuged at 37,500 × g (20,000 rpm) during 15 min. The supernatant was removed and the NPs were washed successively with water and ethanol and dried under vacuum. Blue powder.

IR (KBr): $\nu(O-H)$ = 3655 cm⁻¹ (coordinated water), $\nu(O-H)$ = 3410 cm⁻¹ (crystallized water), $\nu(C\equiv N)$ = 2173 cm⁻¹ ($Cr^{III}-C\equiv N-Ni^{II}$), $\delta(O-H)$ = 1612 cm⁻¹ (crystallized water), $\nu(Cr^{III}-CN)$ = 724 cm⁻¹, $\delta(Cr^{III}-CN)$ = 489 cm⁻¹.

EDS: 2.47/37.19/60.34 (K/Cr/Ni). Formula found: $K_{0.04}Ni[Cr(CN)_6]_{0.64} \cdot 4.1H_2O$.

Elemental analysis calcd (%): C, 19.71; H, 3.50; N, 22.99; found (%): C, 19.22; H, 3.36; N, 22.15.

Post-synthetic functionalization of $K^+/Ni^{2+}/[Cr^{III}(CN)_6]^{3-}$ PBA nanoparticles with 2-aminoanthracene (1@AA). The post-functionalization was performed by mixing the pristine $K^+/Ni^{2+}/[Cr^{III}(CN)_6]^{3-}$ NPs (30 mg, 0.15 mmol) with the 2-aminoanthracene (145 mg, 0.75 mmol) in ethanol for 24 h under stirring. Then, the solution was centrifuged at 37,500 × g (20,000 rpm) during 15 min. The supernatant was removed and the NPs were washed with ethanol several times. The NPs were dispersed in 10 mL of ethanol to perform a 2-days dialysis using SnakeSkin Dialysis Tubing. Finally, the solid was recovered by centrifugation at 37,500 × g (20,000 rpm) during 15 min and dried under vacuum. Yellow-brown solid.

IR (KBr): $\nu(O-H)$ = 3650 cm⁻¹ (coordinated water), $\nu(O-H)$ = 3400 cm⁻¹ (crystallized water/primary alcohol groups), $\nu(C\equiv N)$ = 2173 cm⁻¹ ($Cr^{III}-C\equiv N-Ni^{II}$), $\nu(C-H)$ = 1640 cm⁻¹ (N-H amine), $\delta(O-H)$ = 1611 cm⁻¹ (crystallized water), $\nu(C-C)$ = 1485-1410 cm⁻¹ (aromatic), $\nu(C-H)$ = 1346-581 cm⁻¹ (aromatic), $\delta(Cr^{III}-CN)$ = 494 cm⁻¹.

EDS: 2.14/36.85/61.00 (K/Cr/Ni).

Elemental analysis calcd (%): C, 25.49; H, 3.32; N, 18.36. Found (%): C, 25.43; H, 3.72; N, 18.15.

Estimated formula for 1@AA: $K_{0.04}Ni[Cr(CN)_6]_{0.60}@AA_{0.18} \cdot 3.8H_2O$.

Characterisation methods

Infrared spectroscopy

Infrared spectra were recorded as KBr disks on a PerkinElmer Spectrum two spectrophotometer.

Ultraviolet-visible spectroscopy

UV-Vis spectra were collected on a JASCO V-650 spectrometer in water or ethanol (C = 1 mg/mL).

X-ray powder diffraction

X-ray powder diffraction patterns were recorded in the 2θ interval 5-60° at room temperature with the PANalytical X'Pert Powder diffractometer analytical diffractometer mounted in a Debye-Scherrer configuration and equipped with Cu radiation ($\lambda = 1.5418 \text{ \AA}$).

TGA analysis

Thermogravimetric analyses were obtained with a thermal analyser STA 409 Luxx® (Netzsch) in the range 25 – 500 °C at heating speed of 5 °C.min⁻¹.

Electron microscopy

Transmission Electron Microscopy (TEM) observations were carried out at 100 kV (JEOL 1200 EXII). Samples for TEM measurements were deposited from solutions on copper grids. Nanoparticles' size distribution histograms were determined using enlarged TEM micrographs taken at magnification of 100 K on a statistical sample of ca. 300 nanoparticles.

Scanning Electronic Microscopy (EDS) analyses were performed on a FEI Quanta FEG 200 instrument. The powders were deposited on an adhesive carbon film and analysed under vacuum. The quantification of the heavy elements was carried out with the INCA software, with a dwell time of 3 μ s.

Magnetic measurements

Magnetic susceptibility data were collected with a Quantum Design MPMS-XL SQUID magnetometer working in the range 1.8 – 350 K with the magnetic field up to 7 Tesla. The data were corrected for the sample holder and the diamagnetic contributions calculated from the Pascal's constants. The AC magnetic susceptibility measurements were carried out in the presence of a 3 Oe oscillating field in a zero or applied external DC field.

Photoluminescence measurements

The emission and excitation spectra were recorded at 14 K and 295 K using a Fluorolog3® Horiba Scientific (Model FL3-22) spectroscopy, with a modular double grating excitation spectrometer (fitted with a 1200 grooves/mm grating blazed at 330 nm) and a TRIAX 320 single emission monochromator TRIAX 320 single emission monochromator (fitted with a 1200 grooves/mm grating blazed at 500 nm, reciprocal linear density of 2.6 nm mm⁻¹). The excitation source was a 450 W Xe arc lamp. Low temperature measurements (14 K) were performed using a helium-closed cycle cryostat with vacuum system measuring $\sim 5 \times 10^{-6}$ mbar and a temperature controller (Lakeshore 330, auto-tuning). Time-resolved measurements were carried out with the Fluorolog coupled to a TBX-04 photomultiplier tube module (950 V), 200 ns time-to-amplitude converter and 70 ns delay. The exciting source was a Horiba Scientific pulsed diode light source (NanoLED-390, peak at 388 nm).

Absolute emission quantum yield (q) measurements

The q values were measured at room temperature using a system (C9920-02, Hamamatsu) with a 150 W xenon lamp coupled to a monochromator for wavelength discrimination, an integrating sphere as the sample chamber, and a multichannel analyzer for signal detection. The method is accurate to within 10 %.

Computational section

Complementary Monte Carlo simulations were performed at 300 K to determine the saturation loading in amino-anthracene in the PBA structure and the interaction energy between the first molecule and the framework. For that purpose, 5×10^6 steps for equilibration and 5×10^6 steps of production were considered and we combined Universal Force Field (UFF) with partial charges for the molecules and the framework to implement them in the home-made Monte Carlo code. Following the strategy proposed in Rojas et al.,¹ ESP charges were extracted from DMol³ calculations for amino-anthracene while qEq partial charges (corresponding to the partial charges obtained from the electronegativity equalization method) were considered. Regarding the Lennard Jones interactions, the Lorentz-Berthelot rules were applied as well as a cut-off radius equal to 12.5 Å. In addition, Ewald summation for the electrostatic part was handled to increase the convergence for the energy calculations.

The structures considered for the solids have already been presented in the literature.

In addition, classical calculations performed with GULP have been used to optimize the geometry of the solid in chemical interaction with the amino-anthracene in order to compare the physical interaction (similar to adsorption of the molecule) and the chemical interaction (similar to chemisorption of the molecule on the unsaturated metal center). For these calculations, the same parameters used before have been considered.

Keep in mind that the molecular simulations has focused on the microscopic pores and not on the mesopores which were present in the structure. From Monte Carlo simulations, the adsorption enthalpy at low coverage (1 molecule per cell) is estimated at $-21 \text{ kcal.mol}^{-1}$, while the chemical interaction between AA and PBA gives $-27 \text{ kcal.mol}^{-1}$. This value is obtained from the difference between the energy of the {PBA + AA} structure (where the AA is interacting with the Ni²⁺ cation by NH₂) and the sum of the energy of the empty PBA structure and the energy of the AA molecule. These results point out that AA should interact with PBA by strong chemical coordination interactions.

In complement, the pore size distribution has been calculated using the same parametrization for the framework (UFF) and the methodology developed by Gelb and Gubbins.² The pores size distribution shows two different types: the tetrahedral sites of the cfc structure (with pore diameter close to 3.5 Å) and larger pores (with pore diameter estimated at 8 Å from Figure S6 if we consider a spherical ball to probe the porosity, but the pores are elongated and dimensions are close to 8 Å x 8 Å x 11 Å) formed by cyanometallates vacancies which are suitable to accommodate AA of 10 Å x 5 Å x 1 Å.

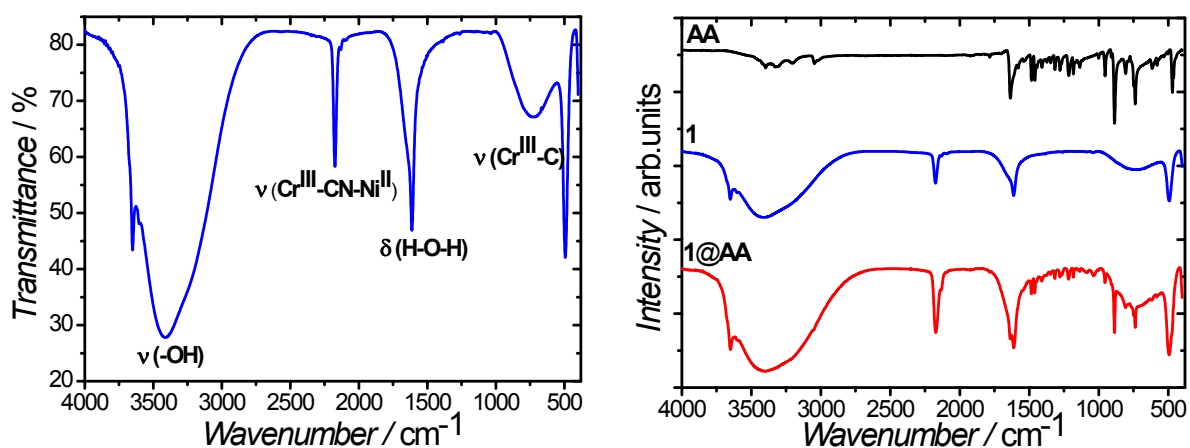


Fig. S1. IR spectra of **1** (left) and comparison between IR spectra of AA, **1** and **1@AA** (right).

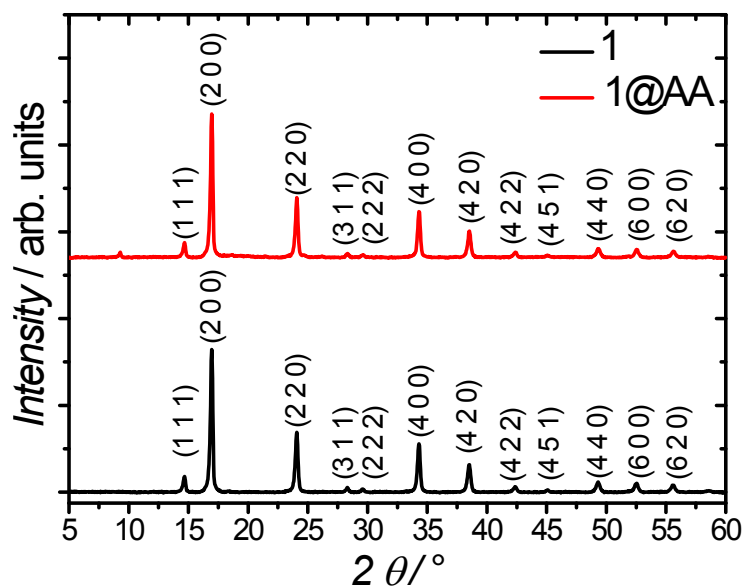


Fig. S2. PXRD patterns of **1** (black) and **1@AA** (red).

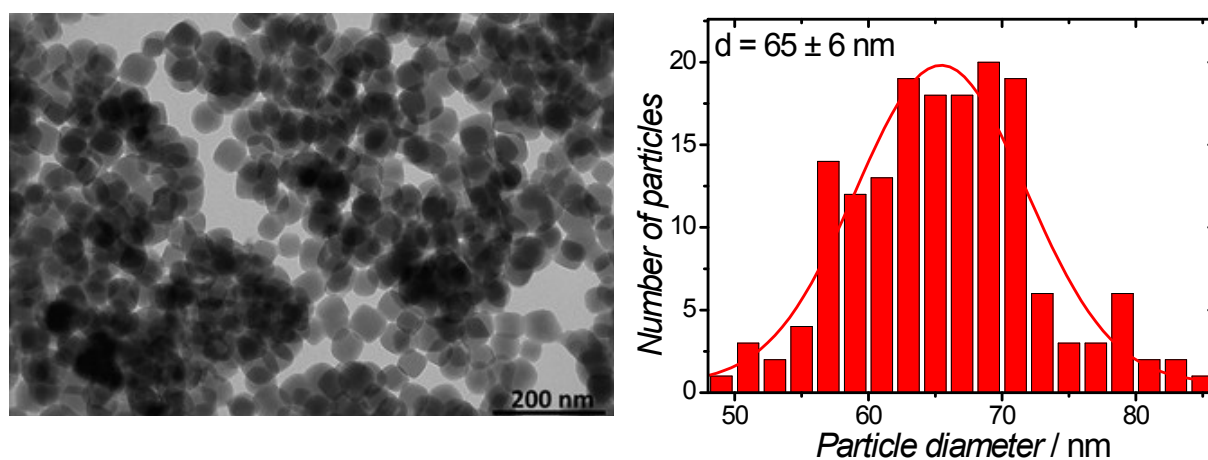


Fig. S3. TEM image (left) and size distribution (right) for **1**.

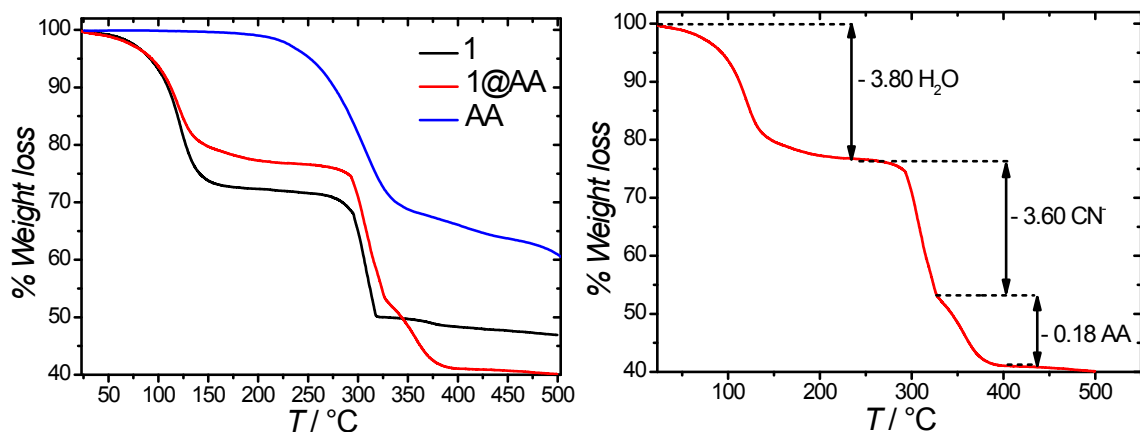


Fig. S4. Left: TGA analysis obtained with a $5^{\circ}\text{C}\cdot\text{min}^{-1}$ heating rate for **1**, **AA** and **1@AA**. Right: TGA curve obtained with a $5^{\circ}\text{C}\cdot\text{min}^{-1}$ heating rate demonstrating the decomposition of **1@AA**.

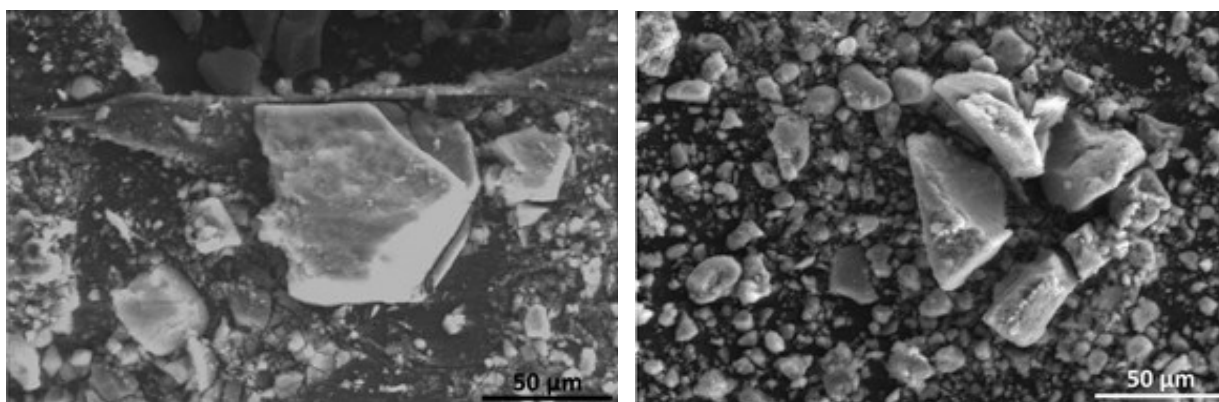


Fig. S5. SEM image for **1** (left) and **1@AA** (right).

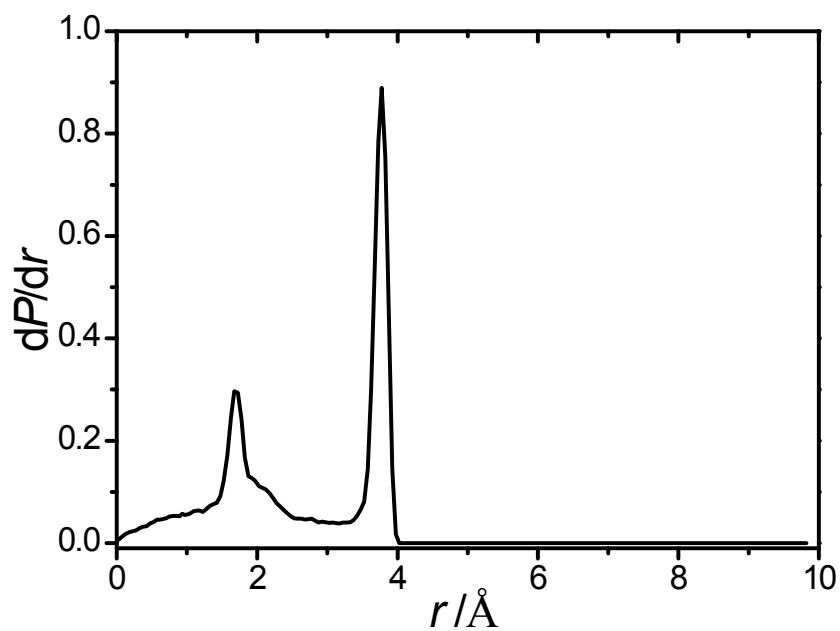


Fig. S6. Pore size distribution of **1** obtained from Monte Carlo simulations illustrating the presence of two types of pores corresponding to the channels and the larger pores formed by the vacancies.

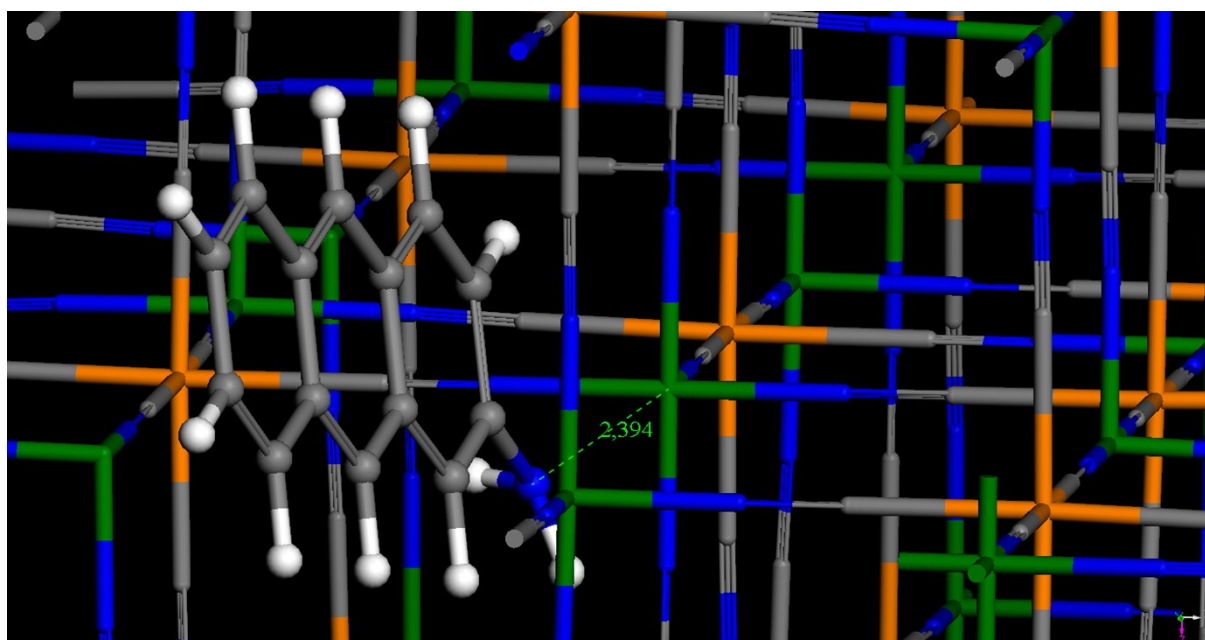
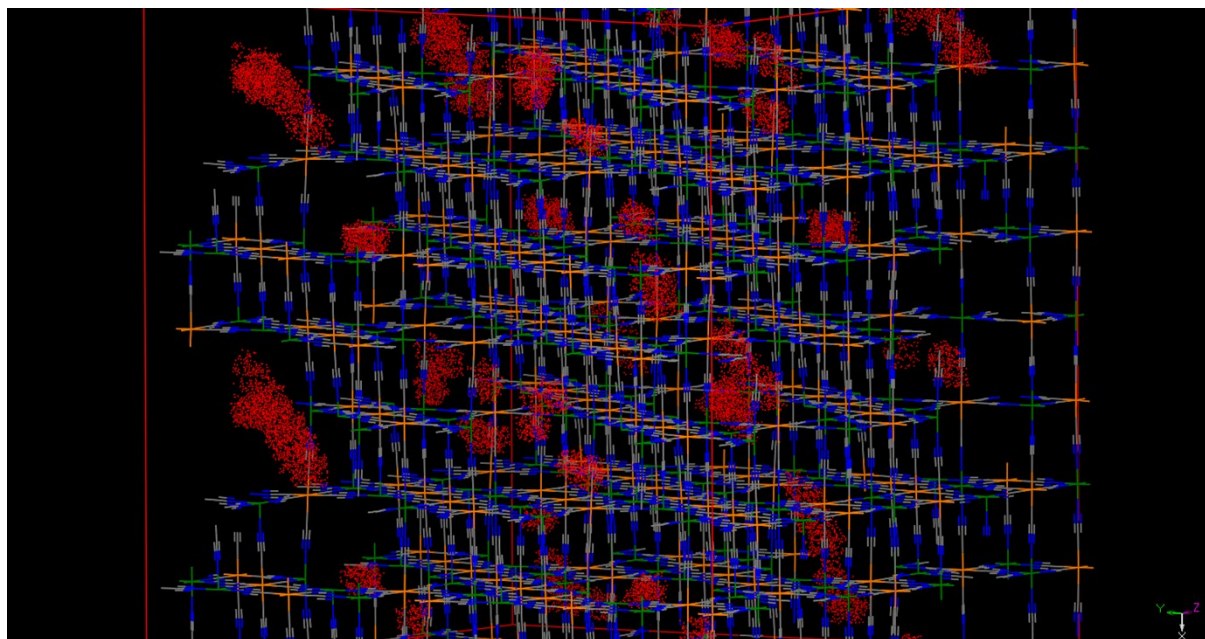


Fig. S7. Top: Snapshot illustrating the density of presence of the AA molecules in the empty PBA structure **1** from Monte Carlo simulations. Bottom: Plausible Configuration of the AA molecule in PBA structure **1** from Monte Carlo simulations at low coverage.

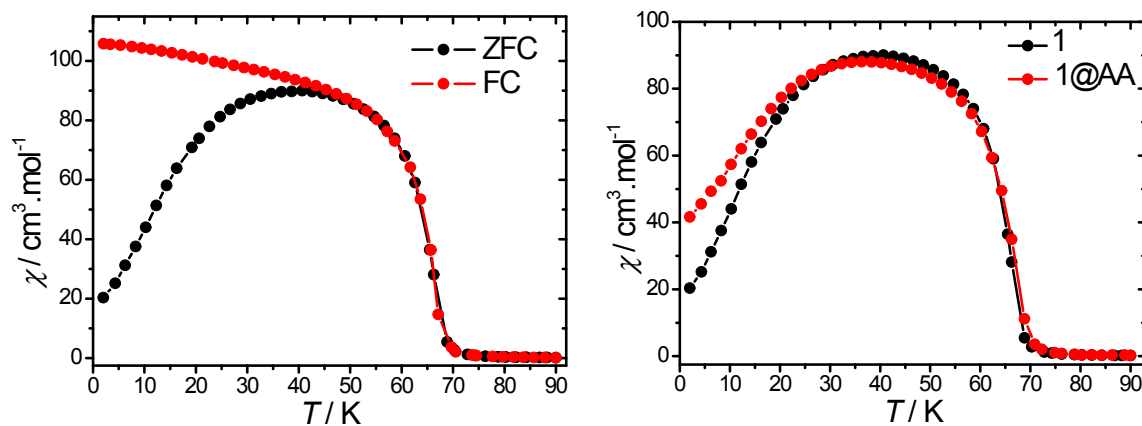


Fig. S8. ZFC/FC curves performed for **1** with an applied magnetic field of 100 Oe (left); ZFC curves performed with an applied magnetic field of 100 Oe for **1** and **1@AA** (right).

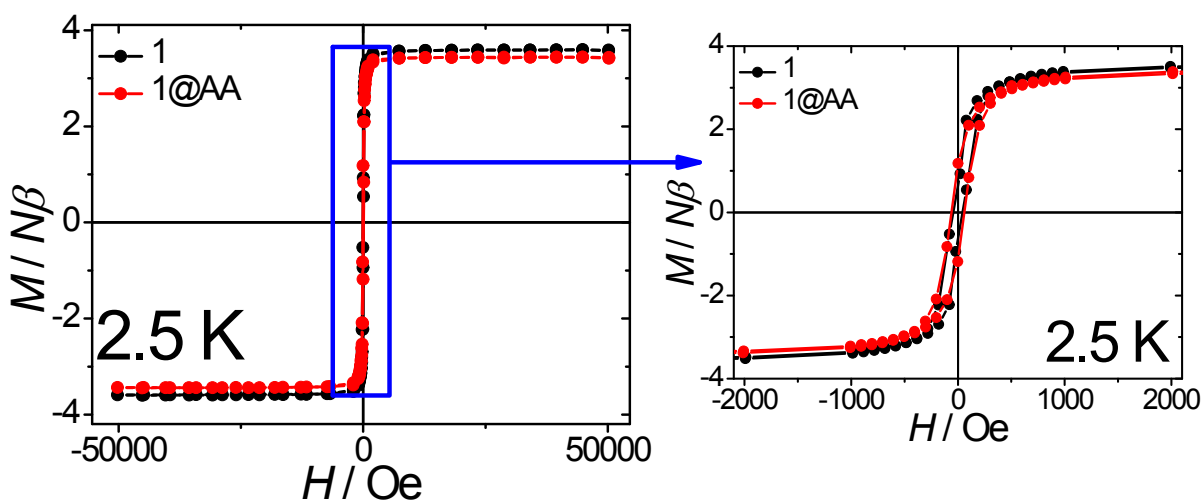


Fig. S9. Field dependence of the magnetization performed at 2.5K for **1** and **1@AA**.

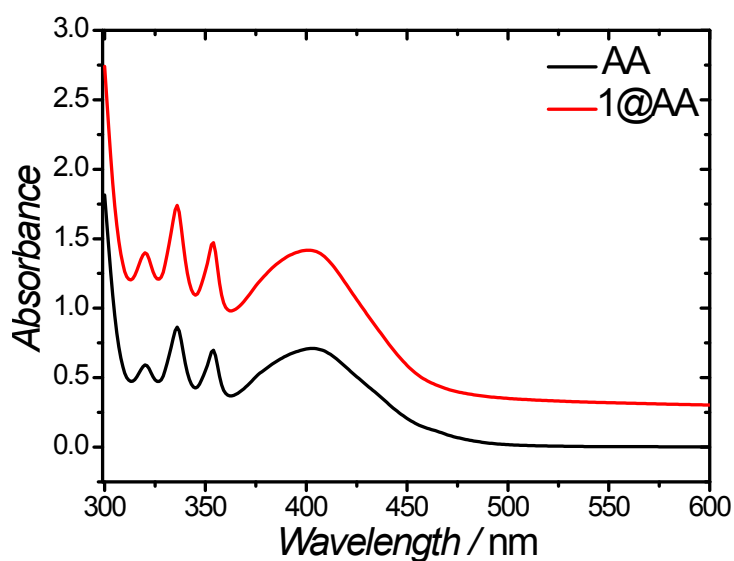


Fig. S10. Room temperature absorption spectra for AA and **1@AA** in ethanol (1 mg/mL).



Fig. S11. Photographs of **1** (left) and **1@AA** (right) re-dispersed in ethanol and excited under a UV lamp, wavelength 365 nm.

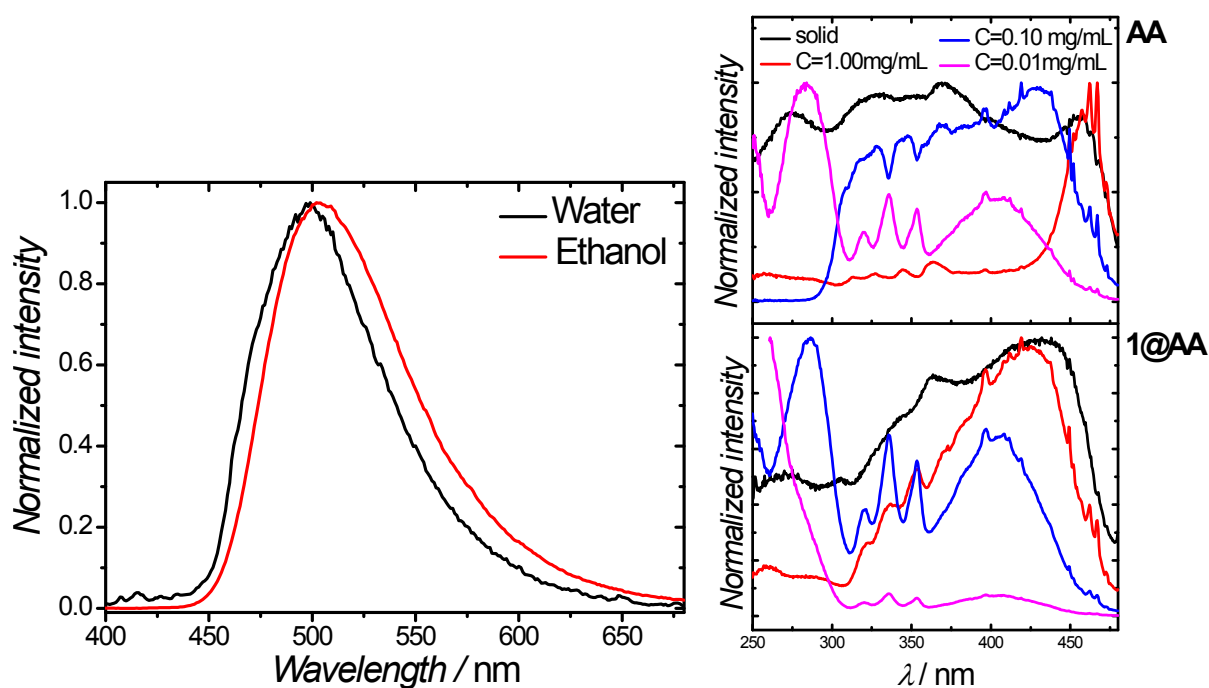


Fig. S12. Left: Room temperature normalized emission spectra for **1@AA** re-dispersed in ethanol or water (1 mg/mL) and excited at 370 nm. Right: Room temperature normalized excitation spectra for AA and **1@AA** re-dispersed at various concentrations in ethanol.

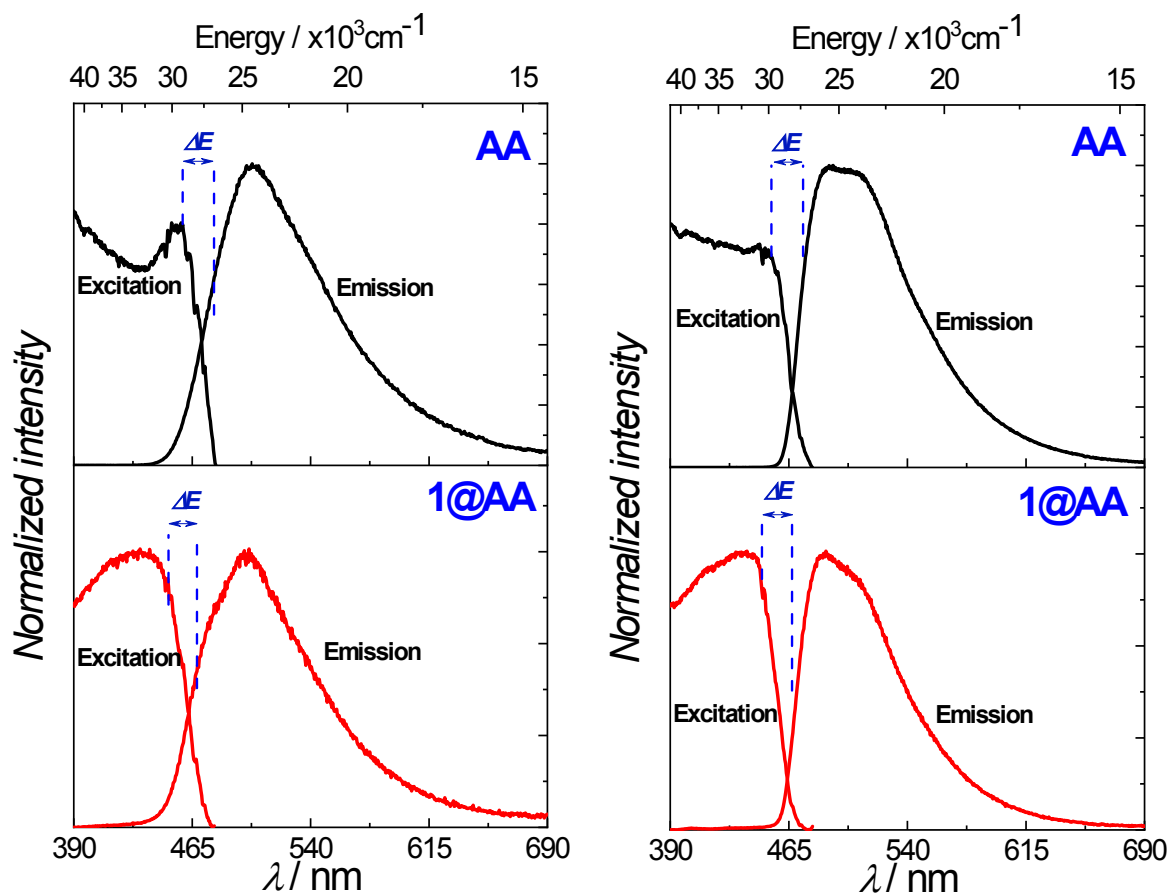


Fig. S13. Excitation and emission spectra monitored around 500 nm and excited at 365 nm, respectively, acquired at (left) 300 K and (right) 16 K for powdered AA and 1@AA; ΔE indicates the energy difference between the high-wavelength component in the excitation spectra and the singlet emitting state.

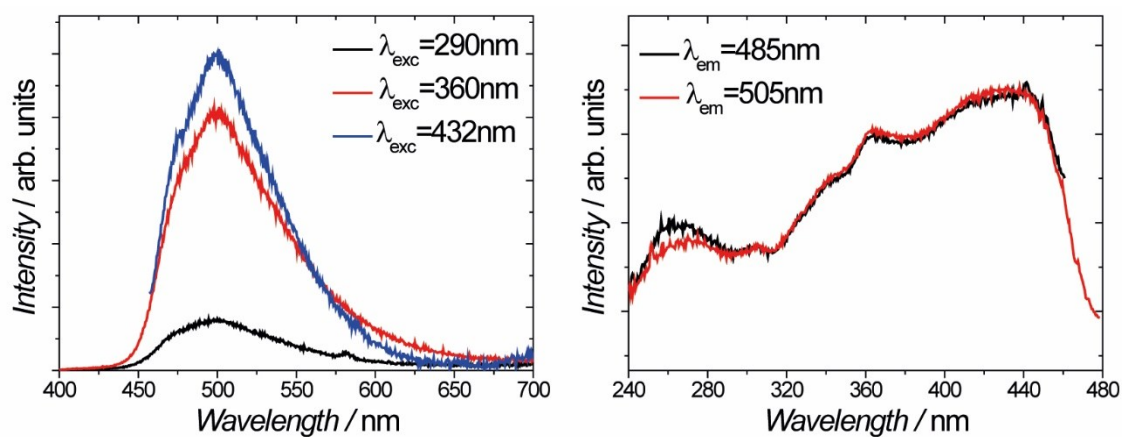


Fig. S14. Room temperature emission (left) and excitation (right) spectra for powdered 1@AA.

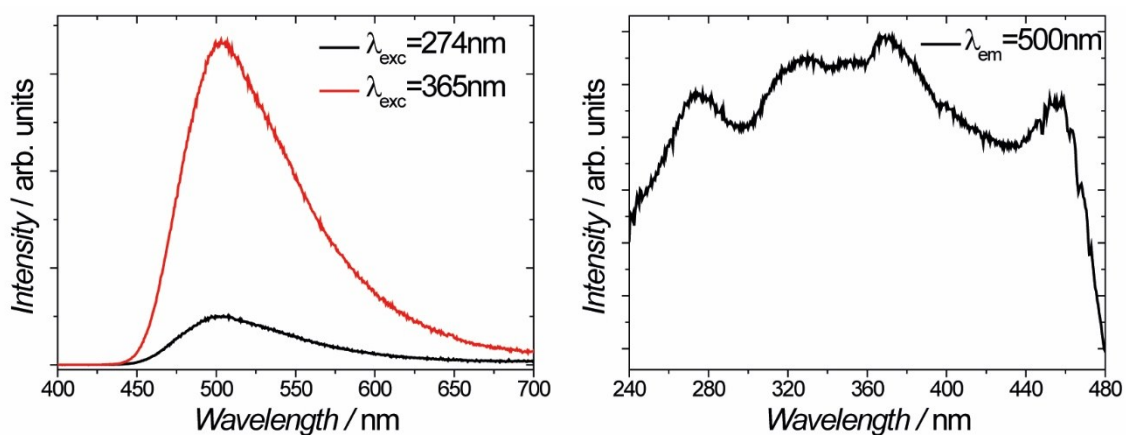


Fig. S15. Room temperature emission (left) and excitation (right) spectra for powdered AA.

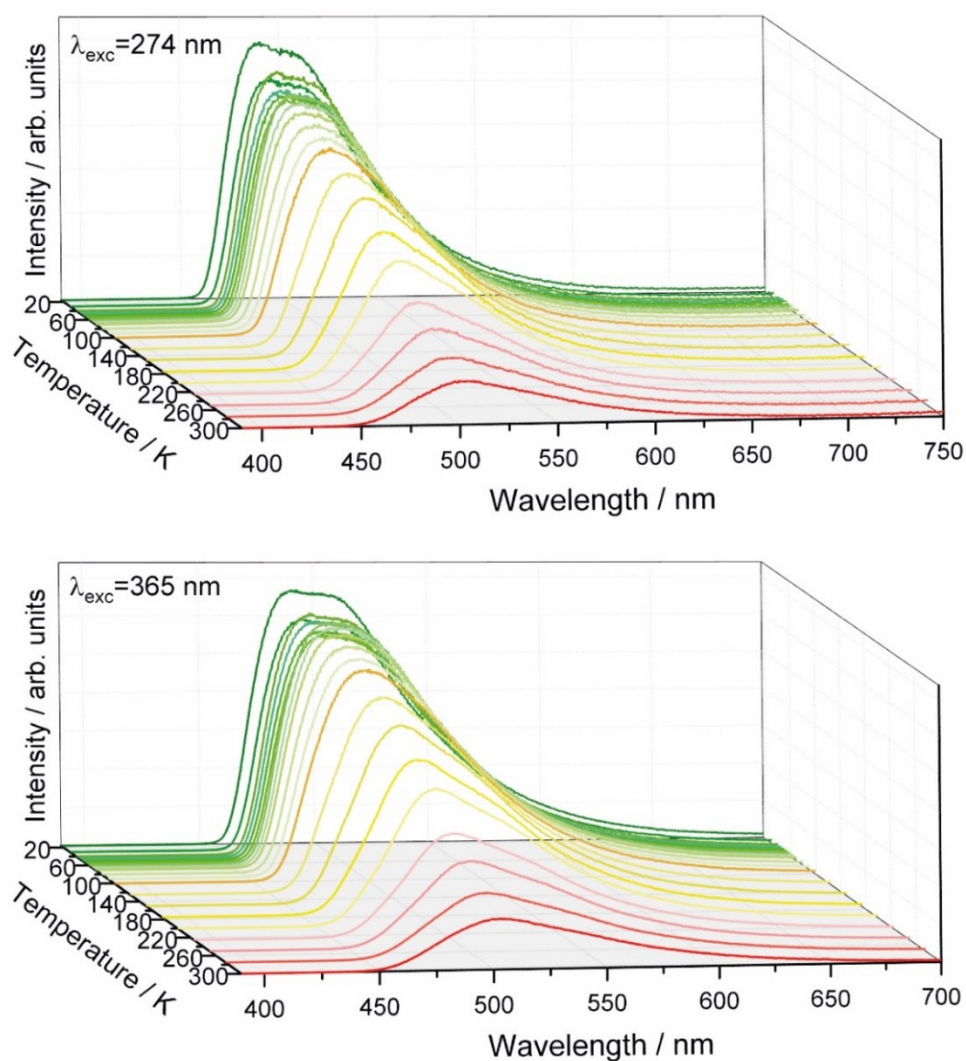


Fig. S16. Emission spectra excited at 274 nm and excited at 365 nm of powdered AA as function of temperature.

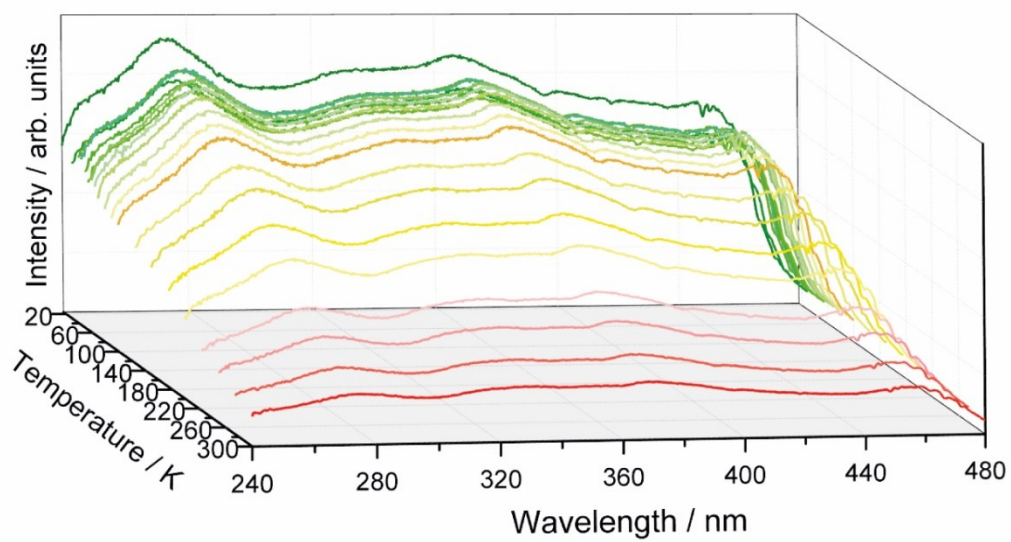


Fig. S17. Excitation spectra monitored at 500 nm of powdered AA as function of temperature

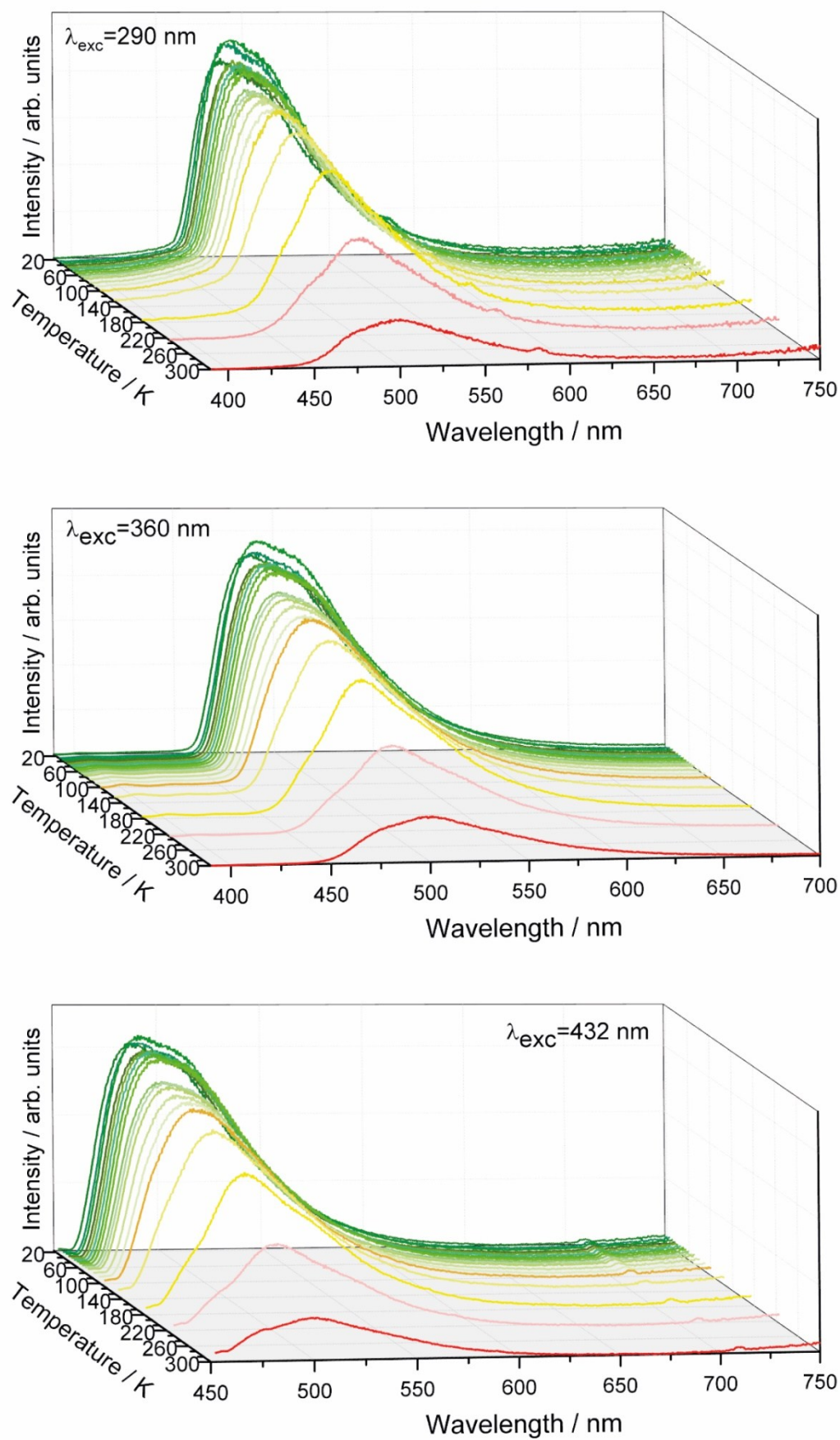


Fig. S18. Emission spectra excited at 290, 360 and 432 nm for powdered 1@AA as function of temperature.

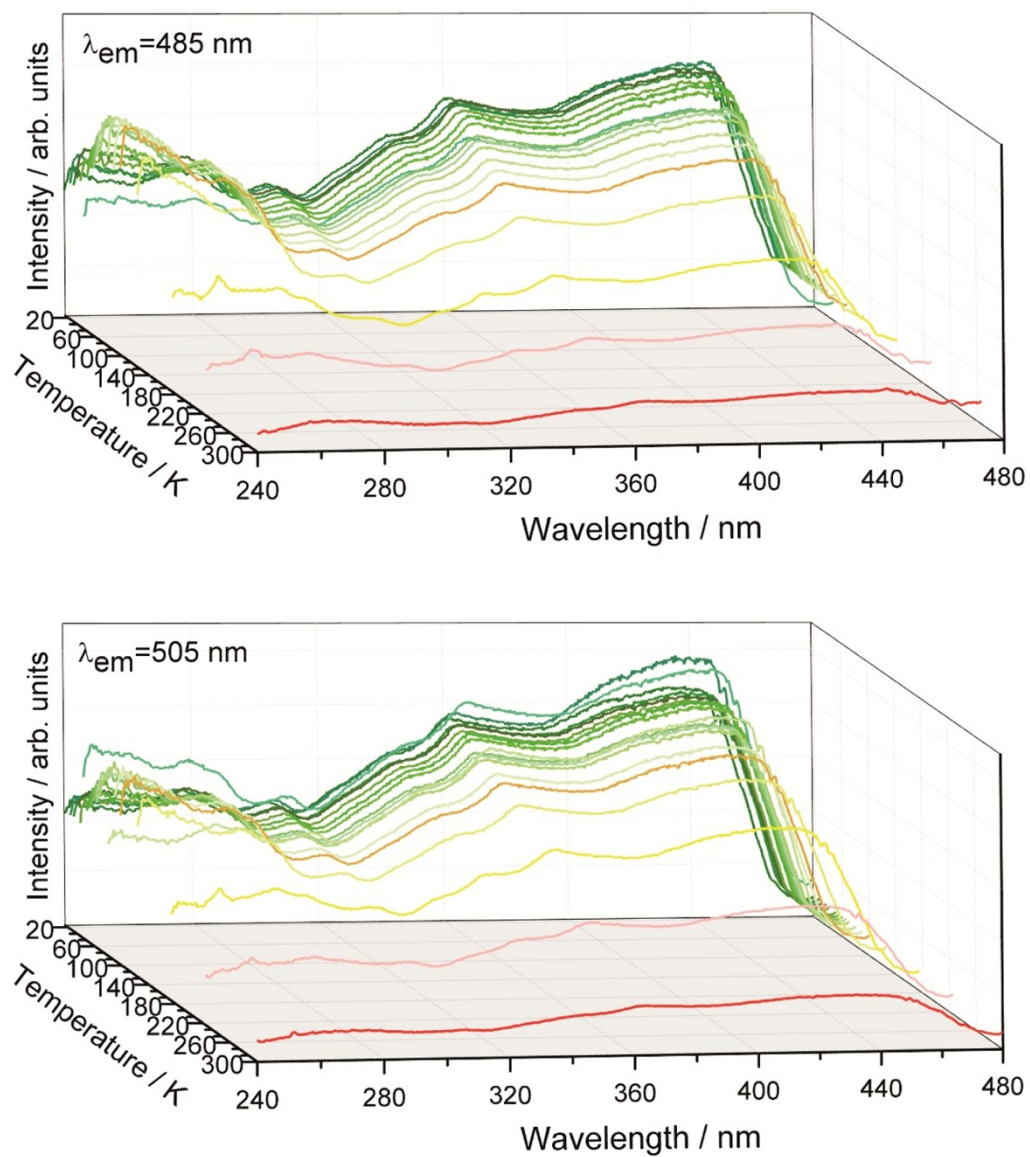


Fig. S19. Excitation spectra monitored at 485 and 505 nm of powdered **1@AA** as function of temperature.

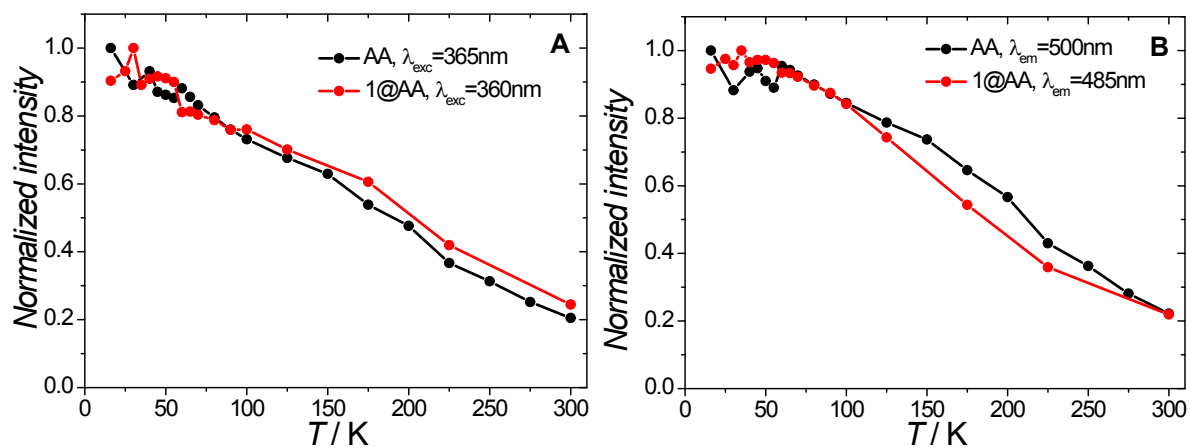


Fig. S20. Integrated intensity of the emission (left) and excitation spectra (right) excited at 360-365 nm and monitored at 485-500 nm, respectively for powdered AA and 1@AA. The solid lines are guide to the eyes.

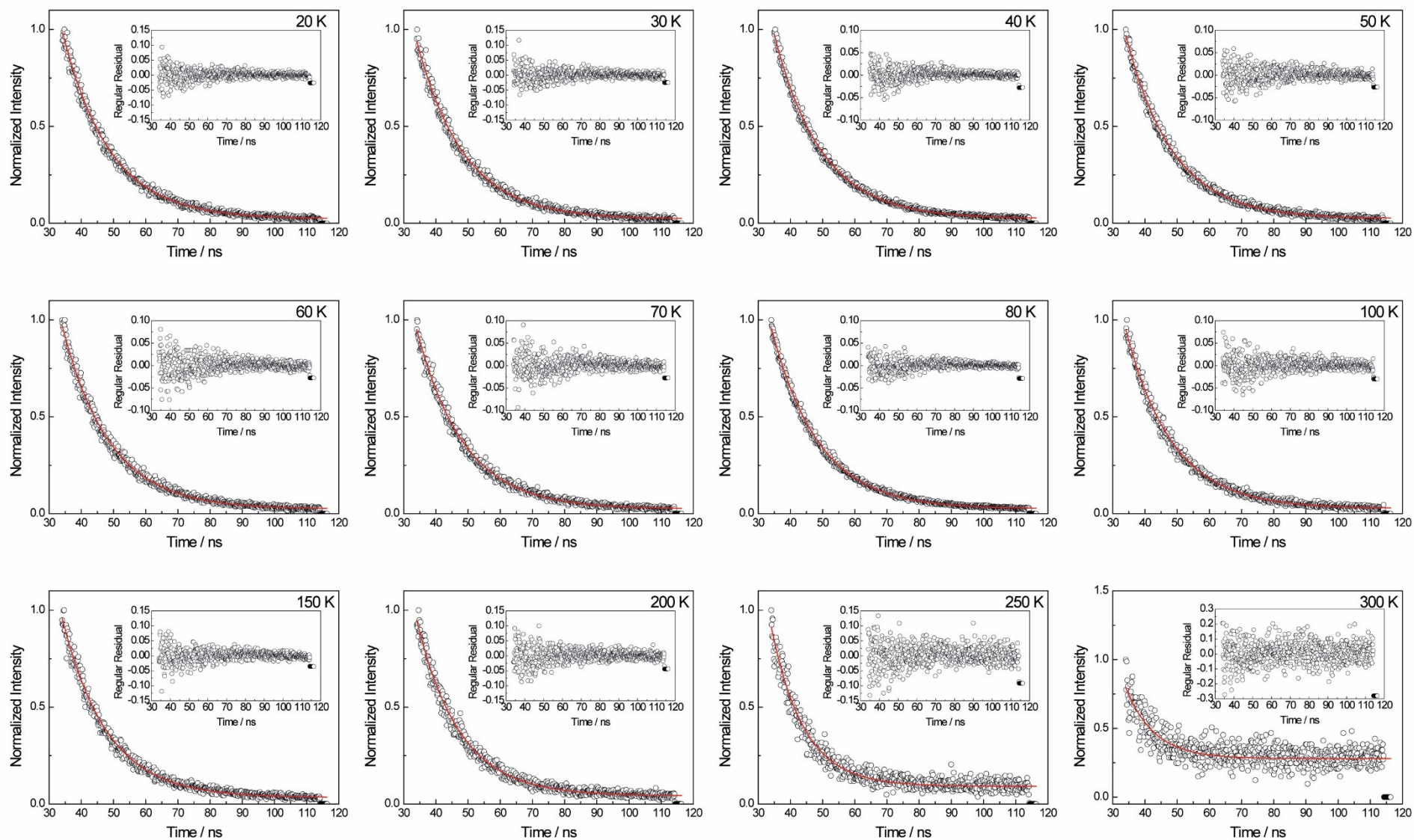


Fig. S21. Emission decay curves of powdered AA monitored at 500 nm as function of temperature. The solid lines represent the data best ($r > 0.9$) fit using a single exponential function. The insets show the fit residual plots.

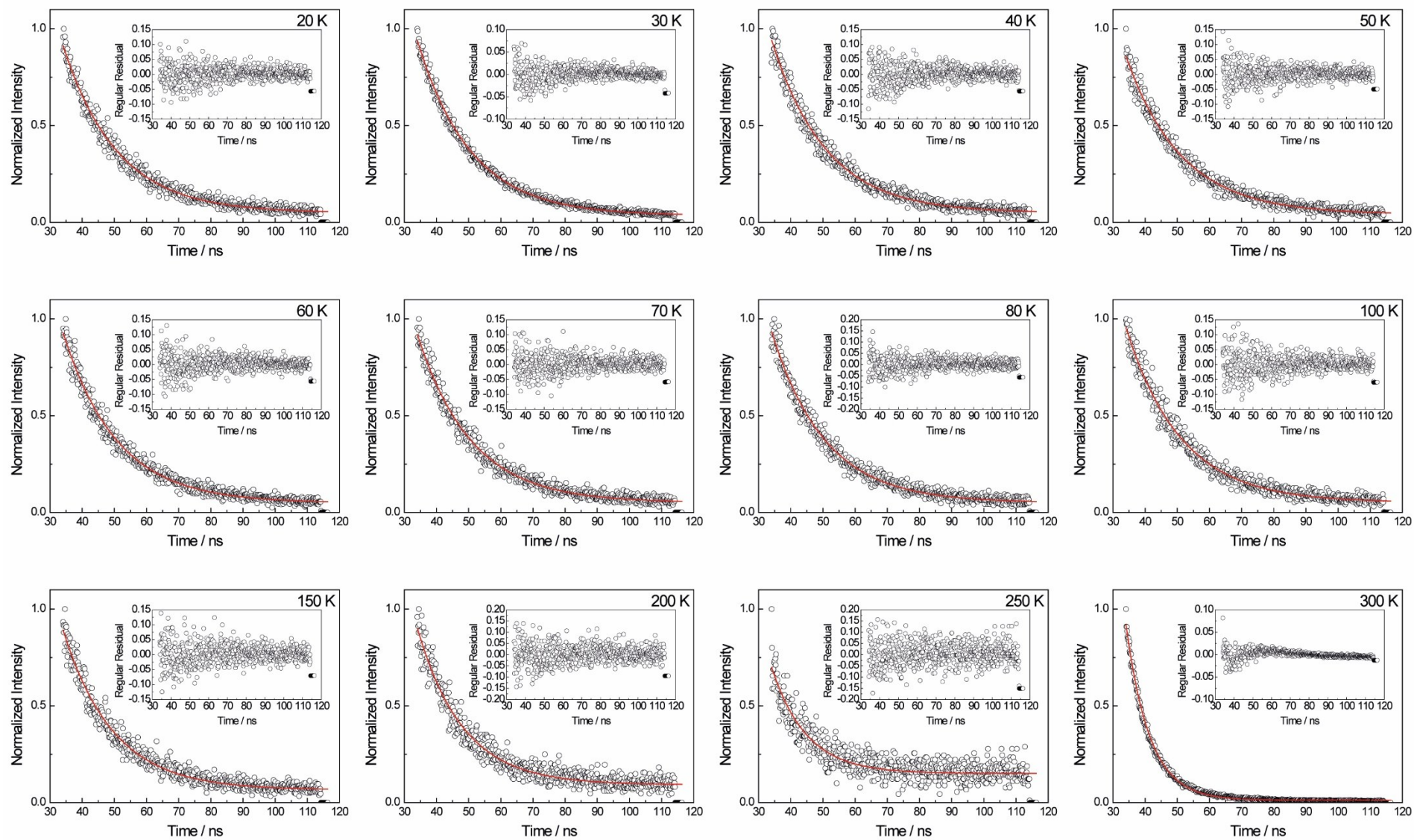


Fig. S22. Emission decay curve of powdered **1@AA** monitored at 500 nm as function of temperature. The solid lines represent the data best ($r > 0.9$) fit using a single exponential function. The insets show the fit residual plots.

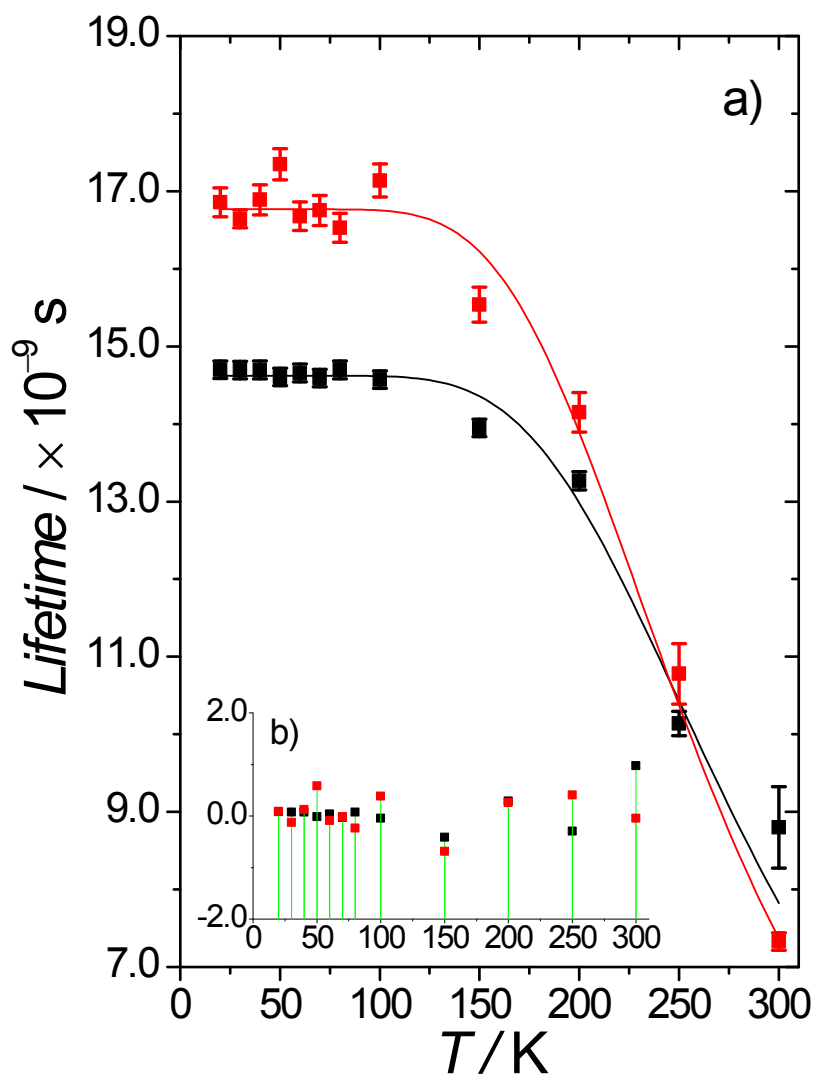


Fig. S23. a) Thermal dependence of the fluorescence lifetime values for powdered AA (black) and 1@AA (red) monitored at 500 nm. The solid lines correspond to the data best fit using the Mott-Seitz model (Equation (1)); b) Fit regular residual plot.

Table S1. Values of the zeta potential for 1 and 1@AA

<i>Sample</i>	<i>Zeta potential (mV)</i>
1	-28 ± 5
1@AA	-29 ± 5

References

- 1 S. Rojas, I. Colinet, D. Cunha, T. Hidalgo, F. Salles, C. Serre, N. Guillou and P. Horcajada, *ACS Omega*, 2018, **3**, 2994-3003.
- 2 L. D. Gelb and K. E. Gubbins, *Langmuir*, 1999, **15**, 305-308.